RSC Advances

PAPER

View Article Online
View Journal | View Issue

Check for updates

Cite this: *RSC Adv.*, 2026, **16**, 22032

Green spectrofluorimetric determination of clemastine using nitrogen and phosphorus Co-doped carbon quantum dots with face-centered design optimization and sustainability assessment

Ahmed A. Almrasy, *[a] Omkulthom Al kamaly [b] and Mustafa Sayedahmed[c]

A novel, environmentally sustainable spectrofluorimetric method was developed for the determination of clemastine fumarate in pharmaceutical formulations and biological matrices using nitrogen and phosphorus co-doped carbon quantum dots (N,P-CQDs) as fluorescent nanoprobes. The N,P-CQDs were synthesized *via* rapid microwave-assisted carbonization of citric acid, urea, and phosphoric acid, yielding uniform nanoparticles (3.2 ± 0.9 nm) with high quantum yield (47.2 ± 2.3%) and strong blue emission at 445 nm. Face-centered central composite design was employed to optimize analytical parameters, achieving optimal conditions at pH 8.7, a buffer volume of 1.5 mL, an N,P-CQD concentration of 175 μg mL^{-1}, and an incubation time of 3 minutes. Mechanistic studies confirmed static fluorescence quenching through ground–state complex formation driven by electrostatic interactions between protonated clemastine and deprotonated carboxyl groups on the nanoprobe surface. The validated method exhibited excellent linearity (0.1–4.0 μg mL^{-1}, r^2 = 0.9997), high sensitivity (LOD = 0.03 μg mL^{-1}), satisfactory accuracy (100.41 ± 1.12%), and high precision (RSD < 2%). Successful application in synthetic pharmaceutical tablets and spiked human plasma samples demonstrated practical applicability, with statistical equivalence to reported HPLC methods. Comprehensive green chemistry assessment using MOGAPI (76), CaFRI (78), BAGI (72.5), and RGB12 (whiteness = 84.3) confirmed outstanding environmental sustainability and balanced analytical performance. The proposed method offers a rapid, cost-effective, and environmentally friendly alternative to conventional chromatographic techniques for clemastine quality control and bioanalytical applications.

Received 5th March 2026
Accepted 21st April 2026

DOI: 10.1039/d6ra01896c

rsc.li/rsc-advances

Open Access Article. Published on 27 April 2026. Downloaded on 5/26/2026 1:16:41 AM.
This article is licensed under a Creative Commons Attribution-NonCommercial 3.0 Unported Licence.

1. Introduction

Carbon quantum dots (CQDs) have emerged as a novel class of zero-dimensional fluorescent nanomaterials since their serendipitous discovery during the purification of single-walled carbon nanotubes.[1] These quasi-spherical nanoparticles, typically measuring less than 10 nm in diameter, have rapidly gained prominence in pharmaceutical analysis owing to their unique combination of physicochemical and optical properties.[2,3] Unlike conventional semiconductor quantum dots, CQDs demonstrate superior biocompatibility, negligible cytotoxicity, excellent aqueous solubility, and resistance to photobleaching, positioning them as eco-friendly alternatives for analytical applications.[4,5] Furthermore, CQDs exhibit remarkable tunable photoluminescence across the ultraviolet to near-infrared spectral range, excitation-dependent emission characteristics, high photostability, and facile surface functionalization capabilities.[6,7] These attributes, combined with cost-effective synthesis routes and chemical inertness, have rendered CQDs particularly attractive for pharmaceutical and biomedical sensing applications.[8,9] Interestingly, heteroatom doping has emerged as a strategic approach to modulate the electronic structure and enhance the fluorescence quantum yield of CQDs.[10,11] The incorporation of electron-rich elements such as nitrogen, phosphorus, sulfur, and boron into the carbon framework introduces additional energy states, increases electron density, and creates surface defects that significantly amplify photoluminescence intensity.[12] Notably, nitrogen and phosphorus co-doped CQDs (N,P-CQDs) have demonstrated synergistic effects, achieving quantum yields exceeding 50% through the collaborative modification of band gaps and generation of multiple active sites.[13,14] These doped CQDs exhibit improved fluorescence stability under diverse pH conditions and ionic strength environments, thereby expanding their analytical utility.[15] The development of multicolor fluorescent CQDs through controlled heteroatom doping has

[a]*Pharmaceutical Analytical Chemistry Department, Faculty of Pharmacy, Al-Azhar University, Nasr City 11751, Cairo, Egypt. E-mail: ahmedalialmrasy8@gmail.com*
[b]*Department of Pharmaceutical Sciences, College of Pharmacy, Princess Nourah bint Abdulrahman University, P.O. Box 84428, Riyadh 11671, Saudi Arabia*
[c]*Analytical Research and Development Department, Benchmark Health Company, Cairo, Egypt*

© 2026 The Author(s). Published by the Royal Society of Chemistry

Open Access Article. Published on 27 April 2026. Downloaded on 5/26/2026 1:16:41 AM. This article is licensed under a Creative Commons Attribution-NonCommercial 3.0 Unported Licence.

further broadened their applicability in bioimaging and multiplex sensing platforms.[16] Consequently, doped CQDs have been successfully employed as highly sensitive fluorescent nanoprobes for the spectrofluorimetric determination of various pharmaceutical compounds, including antibiotics, anticancer agents, and neurological drugs, in both pharmaceutical formulations and complex biological matrices.[17,18]

Clemastine fumarate is a first-generation ethanolamine-derivative H1-antihistamine that competitively antagonizes histamine receptors, providing therapeutic relief from allergic manifestations including rhinitis, urticaria, and pruritus.[19] This antihistamine demonstrates rapid gastrointestinal absorption with peak plasma concentrations attained within 2–4 hours and an elimination half-life of approximately 21 hours.[20] Beyond its conventional antihistaminic applications, clemastine has emerged as a promising therapeutic candidate for neurological disorders, particularly for promoting remyelination in multiple sclerosis (MS). The landmark ReBUILD clinical trial demonstrated that clemastine fumarate significantly reduced visual evoked potential latency in patients with chronic demyelinating optic neuropathy, representing the first randomized controlled evidence of remyelination therapy efficacy in MS.[21] Pharmacokinetic studies revealed moderate oral bioavailability (approximately 39%) with extensive extravascular distribution, necessitating precise dosing optimization for therapeutic efficacy.[20] The expanding therapeutic applications of clemastine, coupled with its complex pharmacokinetic profile, underscore the critical need for robust analytical methodologies capable of accurate quantification in pharmaceutical formulations and biological matrices. Consequently, the development of simple, sensitive, and cost-effective analytical methods for clemastine determination remains essential for pharmaceutical quality assurance, therapeutic drug monitoring, and bioavailability studies.

Several analytical methods have been reported for clemastine determination in pharmaceutical formulations and biological matrices. Ingole *et al.* developed a stability-indicating RP-HPLC method employing a LiChrospher® 100 RP-C8 column (5 μm, 150 × 4.6 mm) with a mobile phase comprising methanol:water containing 0.05% triethylamine (90 : 10 v/v) at a flow rate of 0.8 mL min^{-1} and UV detection at 220 nm.[22] However, this method required high volumes of organic solvents (approximately 90% methanol), lengthy analysis times exceeding 7 minutes, and lacked sensitivity for trace-level determinations in biological matrices. For enhanced sensitivity, Horváth *et al.* reported an LC-MS/MS method for pharmacokinetic studies utilizing liquid–liquid extraction with deuterated clemastine as internal standard and a C18 polymer column, achieving a detection limit of 0.01 ng mL^{-1} with a total run time of 2 minutes.[23] Nevertheless, LC-MS/MS methods are constrained by high instrumentation costs, matrix effects, requirement for specialized expertise, and complex sample preparation protocols. Spectrophotometric approaches have also been employed, including the derivative spectrophotometric method by Bedair *et al.* based on second-derivative UV measurements in methanol-hydrochloric acid solution,[24] and the ion-pair complexation method reported by Abd El-Hay *et al.* utilizing binary complex formation with eosin at 552 nm over the concentration range of 1.25–11.25 μg mL^{-1}.[25] These spectrophotometric methods suffer from limited sensitivity, susceptibility to matrix interferences, and narrow linear ranges. Spectrofluorimetric methods offering improved sensitivity include the NBD-Cl derivatization approach by Abd El-Hay *et al.*, wherein clemastine reacts with 4-chloro-7-nitrobenzofurazan to form a fluorescent derivative measured at emission wavelength 535 nm (excitation 477 nm) over the range of 0.05–0.5 μg mL^{-1},[26] and the recent eosin Y fluorescence quenching method by Abdel-Lateef *et al.* measured at 543.5 nm with a detection limit of 0.045 μg mL^{-1}.[27] While these fluorimetric approaches demonstrate enhanced sensitivity compared to spectrophotometric methods, they require derivatization reagents, exhibit pH-dependent stability, face challenges from background fluorescence interferences, and involve multi-step procedures. Notably, despite the widespread application of CQD-based fluorescent nanoprobes for the determination of various pharmaceutical compounds, no CQD-based analytical method has been reported to date for clemastine determination. The inherent advantages of CQDs as stable, reagent-free nanoprobes, combined with the elimination of chemical derivatization steps, offer a compelling analytical platform for clemastine sensing that has not yet been explored. These limitations underscore the need for simpler, greener, and more sensitive analytical alternatives that eliminate complex derivatization steps while maintaining regulatory compliance.

Hence, the primary objective of this study is to develop a sensitive spectrofluorimetric method utilizing microwave-assisted nitrogen and phosphorus co-doped carbon quantum dots (N,P-CQDs) as fluorescent nanoprobes for clemastine determination in pharmaceutical formulations and spiked plasma samples. The synthesized N,P-CQDs will be characterized using transmission electron microscopy (TEM) for morphological analysis, Fourier-transform infrared spectroscopy (FTIR) for functional group identification and UV-visible and fluorescence spectroscopy for optical properties. The fluorescence quenching mechanism will be elucidated through Stern–Volmer analysis, with thermodynamic parameters ($\Delta H°$, $\Delta S°$, $\Delta G°$) characterization. Critical experimental parameters including pH, buffer volume, N,P-CQD concentration, and incubation time will be systematically optimized using response surface methodology employing face-centered central composite design. The method will be validated following ICH Q2(R2) guidelines encompassing linearity, accuracy, precision, sensitivity, and robustness. Furthermore, selectivity will be assessed against pharmaceutical excipients and plasma interferences. The validated method will be applied to synthetic tablets and compared with reference HPLC methods using appropriate statistical tests. Environmental sustainability will be comprehensively evaluated using Modified Green Analytical Procedure Index (MOGAPI),[28] Carbon Footprint Reduction Index (CaFRI),[29] Blue Applicability Grade Index (BAGI),[30] and RGB12 whiteness[31] metrics to ensure compliance with green analytical chemistry principles. The novelty of this work lies in the integrated analytical platform delivered herein, which represents: the first CQD-based analytical method for

Open Access Article. Published on 27 April 2026. Downloaded on 5/26/2026 1:16:41 AM. This article is licensed under a Creative Commons Attribution-NonCommercial 3.0 Unported Licence.

clemastine determination addressing an unmet analytical need for this therapeutically significant drug; the first bioanalytical validation of a fluorimetric method for clemastine in human plasma extending applicability beyond pharmaceutical formulations; the first systematic FCCCD-based optimization of a fluorimetric method for clemastine revealing critical interaction effects governing analytical performance; and the first comprehensive green chemistry assessment of an analytical method for clemastine determination providing a sustainability benchmark using four complementary metrics.

2. Experimental

2.1. Chemicals and reagents

Clemastine fumarate reference standard (purity 99.2%) was purchased from Sigma-Aldrich (St. Louis, MO, USA). Starting materials for N,P-CQD synthesis including citric acid monohydrate (≥99%), urea (≥99%), and phosphoric acid (85% w/v) were obtained from Piochem (Cairo, Egypt). HPLC-grade solvents including ethanol and acetonitrile were supplied by Merck (Darmstadt, Germany). Quinine sulfate dihydrate employed as quantum yield reference standard was acquired from Sigma-Aldrich (St. Louis, MO, USA). Reagents for buffer preparation including boric acid, glacial acetic acid, and sodium hydroxide, along with sulfuric acid for quantum yield measurements, were procured from El-Nasr Pharmaceutical Chemicals Co. (Cairo, Egypt). Potassium bromide utilized for infrared spectroscopic analysis was sourced from Merck (Darmstadt, Germany). Drug-free human plasma samples were acquired from VACSERA CO. (Giza, Egypt) and maintained at −20 °C until required, then allowed to reach ambient temperature before use. Britton–Robinson buffer solutions were prepared immediately before use by combining equimolar concentrations (0.04 M) of boric acid, glacial acetic acid, and orthophosphoric acid in ultrapure water. The pH was adjusted within the 3.0–9.0 range using standardized 0.2 M sodium hydroxide solution. All pH measurements were confirmed using a calibrated pH electrode with accuracy maintained within ±0.05 pH units.

2.2. Instrumentation

UV-visible absorption spectra (200–800 nm) were recorded on a Shimadzu UV-1800 double-beam spectrophotometer using 1 cm quartz cells. Fluorescence measurements were performed on a Jasco FP-6200 spectrofluorometer equipped with a 150 W xenon lamp. Excitation and emission slit widths were set at 10 nm with a scanning rate of 4000 nm min^{-1}, and emission signals were monitored between 375–650 nm using 1 cm quartz cuvettes. pH measurements were conducted with a Jenway 3505 pH meter calibrated daily with standard buffers. Microwave synthesis was performed in a Tornado domestic microwave oven (1000 W, Egypt). Centrifugation was carried out using a Hettich benchtop centrifuge (Tuttlingen, Germany). Particle morphology was examined by transmission electron microscopy on a JEOL JEM-2100 microscope at 200 kV. Hydrodynamic diameter and zeta potential measurements were determined by a Malvern Zetasizer Nano ZS. Fourier-transform infrared spectra were obtained on a Nicolet iS5 spectrometer (4000–400 cm^{-1}) using KBr pellets. Raman spectra were recorded on a Bruker MultiRAM FT-Raman spectrometer using a 1064 nm laser excitation source.

2.3. Synthesis and characterization of N,P-CQDs

N,P-CQDs were synthesized *via* one-step microwave-assisted carbonization methodology adapted from established protocols.[32,33] Citric acid monohydrate (1.0 g), urea (1.0 g), and phosphoric acid (1.0 mL, 85% w/v) were dissolved in ultrapure water (40 mL) in a 50 mL glass beaker with continuous magnetic stirring for 5 minutes until achieving complete solubilization. The resulting transparent solution was positioned centrally on the rotating platform of a domestic microwave oven operating at 800 W power output to ensure uniform microwave energy distribution. Microwave irradiation was maintained for 5 minutes, during which the reaction mixture underwent progressive color transformation from colorless to pale yellow and finally to dark brown, indicating N,P-CQD formation. Following completion of the reaction and cooling to ambient temperature, the crude mixture was centrifuged at 8000 rpm for 20 minutes to remove large carbonaceous aggregates. The supernatant was recovered and purified through dialysis using cellulose membrane tubing with 1000 Da molecular weight cutoff against ultrapure water over 24 hours, with dialysate renewal every 6 hours. The dialyzed N,P-CQD solution was concentrated by precipitation with chilled ethanol at 1 : 3 (v/v) ratio, followed by centrifugation at 10 000 rpm for 20 minutes. The collected precipitate was washed twice with absolute ethanol to eliminate residual unreacted precursors, then dried under vacuum at 40 °C yielding brown powder. A stock solution (1.0 mg mL^{-1}) was prepared by accurately weighing the dried N,P-CQD powder and reconstituting in ultrapure water, then stored at 4 °C in amber vials under light-protected conditions, maintaining fluorescence stability for at least three months.

The synthesized N,P-CQDs were comprehensively characterized using complementary analytical techniques. Particle morphology and size distribution were assessed *via* transmission electron microscopy following sample preparation by depositing diluted N,P-CQD ethanolic dispersion onto carbon-coated copper grids and air-drying at ambient temperature. Hydrodynamic diameter and polydispersity indices in aqueous suspension were measured by dynamic light scattering at 25 °C. Zeta potential was measured at 25 °C to evaluate the surface charge and colloidal stability of the synthesized N,P-CQDs in aqueous suspension. Surface functional groups were identified through Fourier-transform infrared spectroscopy across the 4000–400 cm^{-1} wavenumber range using N,P-CQD powder homogenized with potassium bromide and compressed into pellet form. Raman spectroscopic analysis was performed to investigate the structural integrity and degree of graphitization of the N,P-CQDs, with the I_D/I_G intensity ratio employed to evaluate the extent of structural defects introduced by heteroatom doping. Optical characterization included UV-visible

 © 2026 The Author(s). Published by the Royal Society of Chemistry

Open Access Article. Published on 27 April 2026. Downloaded on 5/26/2026 1:16:41 AM. This article is licensed under a Creative Commons Attribution-NonCommercial 3.0 Unported Licence.

absorption spectral recording between 200–500 nm employing 1 cm quartz cells, and fluorescence spectroscopic measurements with excitation and emission bandwidths set at 10 nm. Photoluminescence quantum yield was determined using the comparative single-point method with quinine sulfate in 0.1 M sulfuric acid (quantum yield = 0.54) as reference fluorophore. Both samples were excited at 344 nm while maintaining absorbance below 0.1 to avoid inner filter effects. Quantum yield was calculated according to:

$$\mathrm{QY(sample)} = \mathrm{QY(ref)} \times (I(\mathrm{sample})/I(\mathrm{ref})) \times (A(\mathrm{ref})/A(\mathrm{sample})) \times (\eta(\mathrm{sample})/\eta(\mathrm{ref}))^2$$

where I represents integrated fluorescence intensity, A denotes absorbance at excitation wavelength, and η signifies solvent refractive index.

2.4. Optimization of experimental conditions

A face-centered central composite design (FCCCD) was employed to systematically optimize the experimental parameters affecting the fluorescence quenching of N,P-CQDs by clemastine. The experimental design and statistical analysis were performed using Design-Expert software (version 11, Stat-Ease Inc., Minneapolis, MN, USA). Four critical factors were selected for optimization based on preliminary screening studies: buffer pH (factor A), buffer volume (factor B), N,P-CQD concentration (factor C), and incubation time (factor D). Each factor was examined at three levels coded as −1, 0, and +1, corresponding to low, central, and high values, respectively. The factor levels were set as follows: pH ranging from 3 to 9 (low: 3, center: 6, high: 9); buffer volume from 0.25 to 1.5 mL (low: 0.25, center: 0.875, high: 1.5); N,P-CQD concentration from 40 to 200 μg mL^{-1} (low: 40, center: 120, high: 200); and incubation time from 3 to 15 minutes (low: 3, center: 9, high: 15). The face-centered design with $\alpha = 1$ was selected to maintain all experimental points within the safe operational range while enabling quadratic model fitting.

The complete experimental design comprised 27 runs including factorial points, axial points, and three center point replicates to estimate pure error and assess model reproducibility (Table S1). The center point conditions were pH 6.0, buffer volume 0.875 mL, N,P-CQD concentration 120 μg mL^{-1}, and incubation time 9 minutes. The experiments were conducted in randomized order to minimize systematic errors and eliminate bias from uncontrolled variables. For each experimental run, Britton-Robinson buffer was prepared by mixing equimolar concentrations of boric acid, acetic acid, and phosphoric acid (0.04 M each), with pH adjustment achieved using sodium hydroxide solution. The specified volume of buffer at the designated pH was transferred to a 10 mL volumetric flask, followed by addition of the appropriate volume of N,P-CQD stock solution to achieve the target concentration. A fixed concentration of clemastine standard solution (4.0 μg mL^{-1}) was then added, and the mixture was incubated for the specified time at ambient temperature (25 ± 2 °C). After incubation, the solution was diluted to volume with distilled water and mixed thoroughly. Fluorescence intensity was measured at excitation wavelength of 345 nm and emission wavelength of 445 nm with slit widths of 10 nm. A blank solution containing all components except clemastine was prepared and measured under identical conditions for each run.

The response variable was the fluorescence intensity ratio (F_0/F), where F_0 and F represent the fluorescence intensities in the absence and presence of clemastine, respectively. All measurements were performed in triplicate, and mean values were used for analysis. The experimental data were subjected to analysis of variance (ANOVA) and fitted to a second-order polynomial equation:

$$Y = \beta_0 + \Sigma\beta_i x_i + \Sigma\beta_{ii} x_i^2 + \Sigma\beta_{ij} x_i x_j$$

where Y is the predicted response, β_0 is the intercept, β_i, β_{ii}, and β_{ij} are the linear, quadratic, and interaction coefficients, respectively, and x_i and x_j are the coded factor values. Insignificant terms ($p > 0.05$) were eliminated to obtain a reduced quadratic model. Model adequacy was evaluated using R^2, adjusted R^2, predicted R^2, adequate precision, and lack-of-fit test. Response surface and contour plots were generated to visualize factor effects and interactions. Numerical optimization using the desirability function determined the optimal factor combination for maximum fluorescence quenching.

2.5. Analytical method development

The optimized experimental conditions derived from the face-centered central composite design were employed for all subsequent analytical determinations. Into a series of 10 mL volumetric flasks, 1.5 mL of Britton–Robinson buffer (pH 8.7) was transferred, followed by addition of an appropriate volume of N,P-CQD stock solution to achieve a final concentration of 175 μg mL^{-1}. Aliquots of clemastine working standard solutions or sample solutions were then added to provide final concentrations in the range of 0.1–4.0 μg mL^{-1}. The mixtures were allowed to equilibrate at ambient temperature (25 ± 2 °C) for 3 minutes with gentle swirling. After incubation, the solutions were diluted to volume with distilled water and mixed thoroughly. Fluorescence intensity measurements were performed immediately using excitation wavelength of 345 nm and emission wavelength of 445 nm with both slit widths set at 10 nm. A reagent blank containing all components except clemastine was prepared and measured under identical conditions to obtain the initial fluorescence intensity (F_0). The quenching of N,P-CQD fluorescence intensity (F) in the presence of clemastine was measured, and the fluorescence intensity ratio (F_0/F) was calculated.

2.6. Application to pharmaceutical formulations

The validated method was applied to the determination of clemastine in synthetic tablet formulations to assess its applicability for pharmaceutical analysis. Synthetic tablets were prepared by mixing accurately weighed amounts of clemastine fumarate with common pharmaceutical excipients including microcrystalline cellulose (60 mg) as filler-binder, lactose monohydrate (30 mg) as filler, croscarmellose sodium (5 mg) as

Open Access Article. Published on 27 April 2026. Downloaded on 5/26/2026 1:16:41 AM. This article is licensed under a Creative Commons Attribution-NonCommercial 3.0 Unported Licence.

disintegrant, magnesium stearate (2 mg) as lubricant, and colloidal silicon dioxide (3 mg) as glidant to simulate typical tablet compositions. The mixture was homogenized thoroughly in a mortar to ensure uniform distribution. An aliquot of the synthetic tablet powder equivalent to 10 mg clemastine was accurately transferred to a 100 mL volumetric flask and extracted with 50 mL ethanol under ultrasonication for 15 minutes to ensure complete drug dissolution. The mixture was allowed to cool to room temperature, diluted to volume with ethanol, and mixed thoroughly. The extract was filtered through Whatman no. 42 filter paper to remove insoluble excipients, and the first portion of the filtrate was discarded. Appropriate aliquots of the clear filtrate were further diluted with ethanol to obtain working solutions within the validated linearity range (0.1–4.0 μg mL^{-1}). The analysis was performed following the general analytical procedure described in Section 2.5, with measurements conducted in triplicate. Recovery percentages were calculated by comparing the determined concentrations against the known amount of clemastine added to the synthetic formulations.

2.7. Application to spiked plasma samples

Blank human plasma samples were equilibrated to room temperature and subjected to vortex mixing for 30 seconds to achieve uniform consistency. Clemastine standard solution was added to separate plasma aliquots to prepare spiked samples at four concentration levels: 0.2, 0.5, 1.0, and 2.0 μg mL^{-1}. Protein precipitation was performed by adding 2 mL of ice-cold acetonitrile to each plasma aliquot, followed by intense vortex mixing for 2 minutes to ensure complete protein denaturation. The resulting mixtures were subjected to centrifugation at 10 000 rpm for 10 minutes under refrigerated conditions (4 °C) to achieve phase separation. The supernatant layers were carefully collected and transferred to clean glass tubes, then evaporated to complete dryness under a gentle stream of nitrogen gas at 40 °C. The dried residues were reconstituted in 500 μL of ethanol with vigorous vortex agitation for 1 minute to ensure complete dissolution. The reconstituted solutions were passed through 0.22 μm syringe filters to remove any particulate matter. The filtered extracts were analyzed according to the general analytical procedure outlined in Section 2.5, with fluorescence measurements performed in triplicate for each concentration level. Recovery percentages were calculated by comparing the experimentally determined concentrations with the theoretical spiked concentrations, and results were expressed as mean ± standard deviation.

3. Results and discussion

3.1. Physicochemical and optical characterization of N,P-CQDs

The microwave-assisted synthesis conditions were systematically optimized to maximize photoluminescence quantum yield as the primary response variable. Preliminary screening experiments evaluated the effects of precursor molar ratios (citric acid : urea ranging from 1 : 0.5 to 1 : 3), phosphoric acid concentration (0.5–2.0 mL), microwave power (600–1000 W), and irradiation time (3–10 minutes) on quantum yield efficiency. The optimal conditions—citric acid : urea molar ratio of 1 : 1, phosphoric acid volume of 1.0 mL, microwave power of 800 W, and reaction time of 5 minutes—were selected based on achieving maximum fluorescence intensity and quantum yield. Citric acid serves as an ideal carbon precursor owing to its abundant hydroxyl and carboxyl functional groups that facilitate both carbonization and surface passivation, while simultaneously providing oxygen-containing functionalities that enhance aqueous solubility. Urea functions as a nitrogen source through thermal decomposition, releasing ammonia that incorporates nitrogen atoms into the carbon lattice *via* C–N bond formation, thereby creating electron-rich sites that modify the band gap structure. Phosphoric acid plays a dual role: it introduces phosphorus heteroatoms that create additional energy levels within the bandgap, and acts as a dehydrating agent that promotes carbonization through elimination of water molecules from citric acid. The synergistic co-doping of nitrogen and phosphorus generates abundant surface defects and active sites that significantly enhance photoluminescence properties. The microwave irradiation method offers distinct advantages over conventional hydrothermal synthesis, including rapid uniform heating through dipolar polarization mechanisms, reduced reaction time from several hours to minutes, improved energy efficiency, and enhanced reproducibility due to precise temperature control. Under the optimized conditions, the photoluminescence quantum yield was determined to be 47.2 ± 2.3%, demonstrating efficient light emission comparable to high-performance heteroatom-doped carbon quantum dots reported in recent literature.

Morphological characterization by transmission electron microscopy revealed that the synthesized N,P-CQDs exhibited quasi-spherical geometry with well-dispersed individual particles and minimal aggregation (Fig. 1A). Statistical analysis of particle dimensions from TEM images indicated an average diameter of 3.2 ± 0.9 nm, consistent with the characteristic size range of carbon quantum dots. Complementary dynamic light scattering measurements provided hydrodynamic diameter data of 3.34 ± 1.24 nm (Fig. S1), confirming the narrow size distribution and monodisperse nature in aqueous suspension. The slight difference between TEM and DLS measurements is attributed to the hydration layer surrounding the particles in solution. The zeta potential of the N,P-CQDs in aqueous suspension was determined to be −24.76 mV (Fig. S2), confirming the presence of abundant negatively charged surface functional groups, particularly deprotonated carboxylate ($-COO^-$) and phosphate moieties, which collectively contribute to the excellent colloidal stability of the nanoprobes. Fourier-transform infrared spectroscopy provided comprehensive evidence of successful nitrogen and phosphorus co-doping along with surface functionalization (Fig. 1B). The broad, intense absorption band spanning 3700–3300 cm^{-1} arose from overlapping O–H stretching vibrations of hydroxyl groups and N–H stretching vibrations of primary and secondary amines, indicating abundant hydrophilic functional groups on the N,P-CQD surface that facilitate aqueous dispersibility. The characteristic peak at approximately 1700 cm^{-1} was assigned to C=O

 © 2026 The Author(s). Published by the Royal Society of Chemistry

Open Access Article. Published on 27 April 2026. Downloaded on 5/26/2026 1:16:41 AM.
This article is licensed under a Creative Commons Attribution-NonCommercial 3.0 Unported Licence.

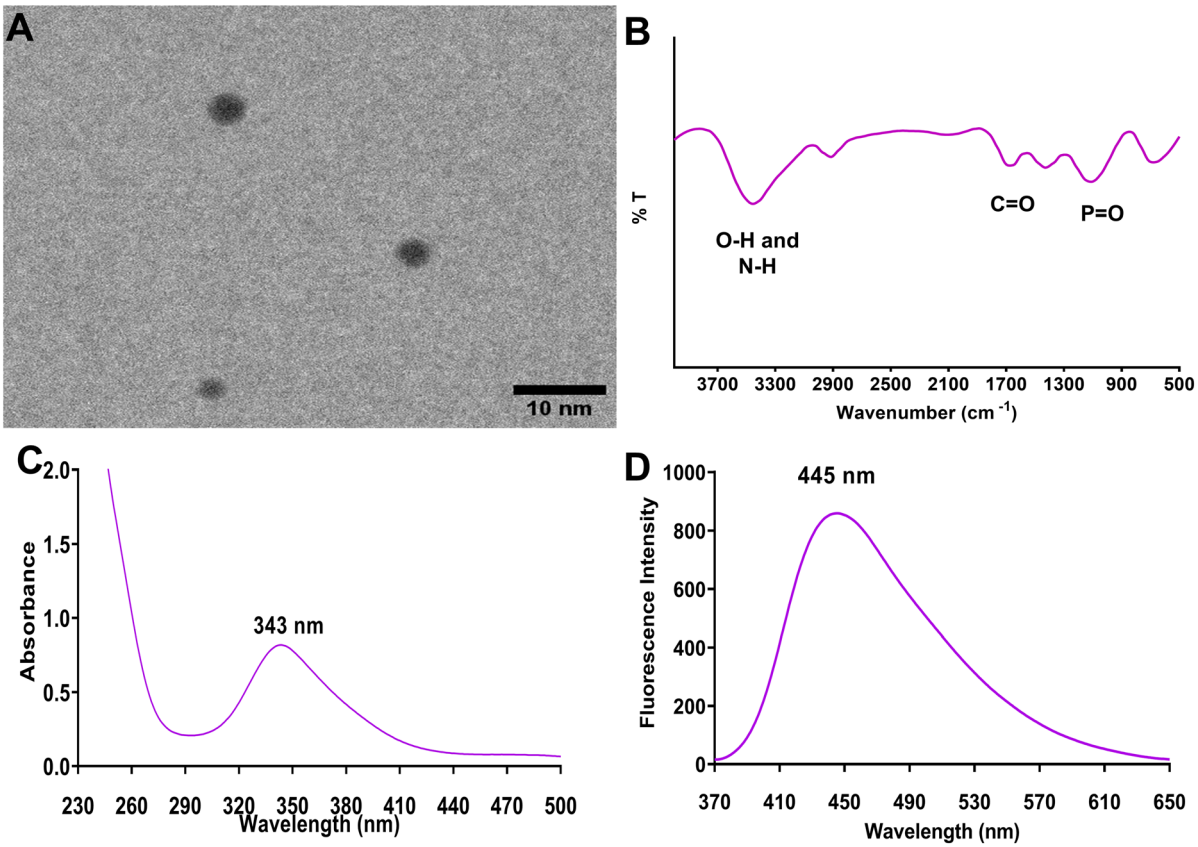

Fig. 1 Physicochemical and optical characterization of nitrogen and phosphorus co-doped carbon quantum dots (N,P-CQDs). (A) Transmission electron microscopy image showing quasi-spherical morphology and uniform size distribution. (B) Fourier-transform infrared spectrum displaying characteristic functional groups including O–H/N–H stretching, C═O stretching, and P═O stretching vibrations, confirming successful nitrogen and phosphorus co-doping and surface functionalization. (C) UV-visible absorption spectrum showing characteristic absorption maximum attributed to n → π* transitions. (D) Fluorescence emission spectrum exhibiting bright blue luminescence with substantial Stokes shift between excitation and emission wavelengths.

stretching vibrations originating from carboxyl (–COOH) and carbonyl (C═O) moieties, confirming the presence of oxygen-containing functional groups derived from citric acid precursor. The absorption band observed near 1300 cm^{-1} corresponded to P═O stretching vibrations, providing direct spectroscopic evidence of phosphorus incorporation into the carbon quantum dot framework. Additionally, peaks in the 1600–1500 cm^{-1} region were attributed to aromatic C═C stretching and N–H bending vibrations, while bands around 1200–1000 cm^{-1} could be assigned to C–N and C–O–C stretching modes. These surface functional groups not only contribute to the excellent water solubility and colloidal stability of N,P-CQDs but also serve as potential binding sites for analyte interactions through hydrogen bonding and electrostatic attractions. Raman spectroscopic analysis further confirmed the carbon nanostructure of the synthesized N,P-CQDs (Fig. S3). Two characteristic bands were observed: the D band at 1355 cm^{-1} arising from structural defects and disordered sp^3 carbon introduced by nitrogen and phosphorus heteroatom incorporation, and the G band at 1548 cm^{-1} corresponding to the in-plane vibrations of graphitic sp^2 carbon domains. The calculated I_D/I_G ratio of 1.01 indicates a defect-rich carbon structure, confirming that N and P co-doping successfully introduced structural disorder into the carbon framework, consistent with the generation of abundant surface defects that serve as radiative recombination centers contributing to the enhanced photoluminescence quantum yield.

Optical characterization revealed distinct photophysical properties suitable for fluorometric sensing applications. The UV-visible absorption spectrum exhibited a characteristic absorption peak at 343 nm (Fig. 1C), attributed to n → π* electronic transitions of carbonyl groups (C═O bonds) present on the N,P-CQD surface. The fluorescence emission spectrum displayed a well-defined maximum emission wavelength at 445 nm when excited at 345 nm (Fig. 1D), corresponding to bright blue luminescence visible under UV illumination. This substantial Stokes shift of approximately 100 nm between excitation and emission wavelengths minimizes self-absorption effects and reduces background interference, thereby enhancing analytical sensitivity. The emission profile exhibited a symmetric Gaussian distribution with a full width at half maximum of approximately 100 nm, indicating relatively uniform electronic states and homogeneous particle size distribution. The observed blue emission originates from

Open Access Article. Published on 27 April 2026. Downloaded on 5/26/2026 1:16:41 AM. This article is licensed under a Creative Commons Attribution-NonCommercial 3.0 Unported Licence.

radiative recombination of photogenerated electron–hole pairs in surface states and quantum confinement effects within the sp^2 carbon core. The photoluminescence quantum yield of 47.2 ± 2.3%, determined using the comparative method with quinine sulfate as reference standard, demonstrates efficient light emission exceeding many conventional fluorophores. This high quantum yield, combined with excellent photostability under continuous UV irradiation, resistance to photobleaching, and superior aqueous dispersibility, rendered the synthesized N,P-CQDs highly suitable as fluorescent nanoprobes for pharmaceutical analysis through fluorescence quenching mechanisms. Furthermore, the long-term storage stability of the N,P-CQD stock solution (1.0 mg mL^{-1}, 4 °C, amber vials, light-protected conditions) was confirmed by monitoring fluorescence emission intensity at 445 nm over twelve weeks. The nanoprobes retained 98.6 ± 1.2%, 97.3 ± 1.5%, 96.8 ± 1.8%, and 95.7 ± 2.1% of their initial fluorescence intensity after 2, 4, 8, and 12 weeks, respectively ($n = 3$), with no observable precipitation or spectral shift, confirming satisfactory stability for at least three months under the specified storage conditions. These attributes, combined with excellent aqueous dispersibility, rendered the synthesized N,P-CQDs highly suitable as fluorescent nanoprobes for pharmaceutical analysis through fluorescence quenching mechanisms.

3.2. Fluorescence quenching mechanism and thermodynamic studies

The progressive decrease in N,P-CQD fluorescence intensity upon incremental addition of clemastine (Fig. 2A) demonstrated concentration-dependent quenching behavior, necessitating investigation of the underlying interaction mechanism. As a preliminary control, clemastine alone (4.0 μg mL^{-1}) exhibited negligible intrinsic fluorescence across the 375–625 nm emission range (Fig. S4), confirming that all observed quenching responses originate exclusively from the N,P-CQD nanoprobes. Several potential quenching mechanisms were evaluated to elucidate the nature of the N,P-CQD-clemastine interaction. The inner filter effect, wherein the analyte absorbs excitation or emission light thereby reducing observed fluorescence, was excluded based on the negligible overlap between clemastine absorption spectrum and the N,P-CQD excitation/emission wavelengths (345/445 nm). Furthermore, all absorbance values were maintained below 0.05 throughout the quenching experiments to avoid inner filter artifacts. Förster resonance energy transfer (FRET) was ruled out as

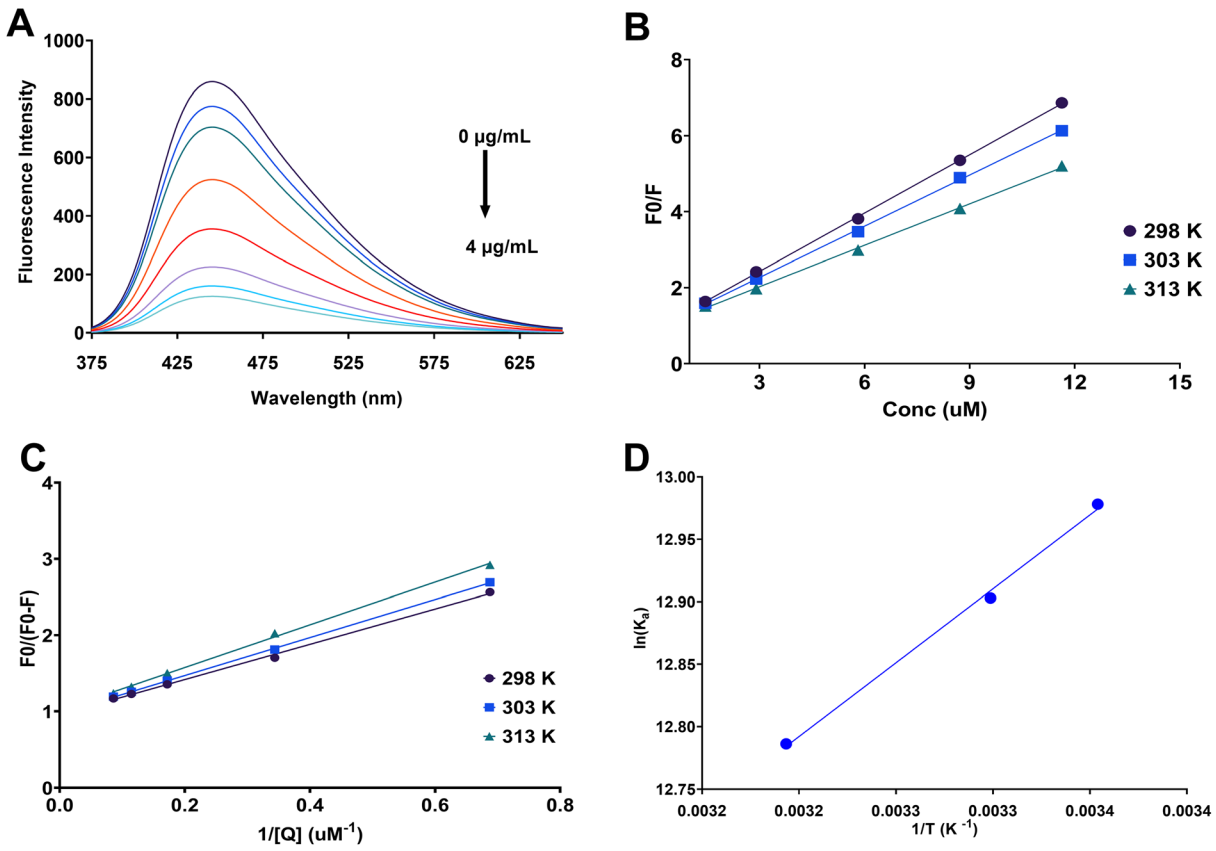

Fig. 2 Fluorescence quenching mechanism and thermodynamic characterization of N,P-CQD-clemastine interaction. (A) Progressive fluorescence quenching of N,P-CQDs upon incremental addition of clemastine, demonstrating concentration-dependent quenching behavior. (B) Stern–Volmer plots at three temperatures showing linear relationships with temperature-dependent slopes for mechanism identification. (C) Modified Stern–Volmer plots for determination of association constants (K_a) at different temperatures. (D) Van't Hoff plot (ln K_a *versus* 1/*T*) for thermodynamic parameter calculation including enthalpy change ($\Delta H°$) and entropy change ($\Delta S°$).

© 2026 The Author(s). Published by the Royal Society of Chemistry

Open Access Article. Published on 27 April 2026. Downloaded on 5/26/2026 1:16:41 AM. This article is licensed under a Creative Commons Attribution-NonCommercial 3.0 Unported Licence.

a quenching pathway due to the absence of spectral overlap between N,P-CQD emission and clemastine absorption, and the lack of distance-dependent energy transfer characteristics.

To differentiate between static and dynamic quenching mechanisms, fluorescence quenching studies were conducted at three different temperatures (298, 303, and 313 K). Classical Stern–Volmer analysis was employed by plotting F_0/F *versus* clemastine concentration, where F_0 and F represent fluorescence intensities in the absence and presence of quencher, respectively (Fig. 2B). The linear Stern–Volmer plots at all temperatures confirmed that the quenching process followed first-order kinetics according to the equation:

$$F_0/F = 1 + K_{sv}[Q]$$

where K_{sv} is the Stern–Volmer quenching constant and [Q] is the quencher concentration. Critically, the Stern–Volmer constant exhibited an inverse temperature dependence, decreasing from 4.3×10^5 M^{-1} at 298 K to 4.0×10^5 M^{-1} at 303 K, and further to 3.6×10^5 M^{-1} at 313 K (Table 1). This progressive reduction in K_{sv} values with increasing temperature, manifested as decreasing slopes in the Stern–Volmer plots (Fig. 2B), is consistent with a static quenching mechanism. In dynamic quenching, elevated temperatures increase molecular collision frequency and diffusion rates, thereby enhancing quenching efficiency and K_{sv} values. Conversely, static quenching involves ground–state complex formation between fluorophore and quencher, which becomes thermodynamically less favorable at higher temperatures due to complex dissociation, resulting in decreased K_{sv} values. The observed inverse temperature relationship strongly suggests that clemastine quenches N,P-CQD fluorescence predominantly through static quenching *via* ground–state complex formation rather than collisional dynamic quenching. To further support this conclusion through direct spectroscopic evidence, UV-visible absorption spectra of N,P-CQDs, clemastine, and their mixture were recorded under the optimized analytical conditions. The absorption spectrum of the N,P-CQD-clemastine mixture revealed a distinct hyperchromic effect accompanied by a bathochromic shift of the characteristic N,P-CQD absorption peak from 343 nm to approximately 350 nm compared to the individual component spectra (Fig. S5). These spectral perturbations are unambiguous signatures of ground–state complex formation between clemastine and the N,P-CQD surface functional groups, providing spectroscopic evidence consistent with ground–state complex formation and supporting the static quenching interpretation.

The binding affinity between N,P-CQDs and clemastine was quantified using the modified Stern–Volmer equation by plotting $F_0/(F_0 - F)$ *versus* 1/[Q] (Fig. 2C), yielding the association constant (K_a) from the ratio of intercept to slope. The association constants similarly decreased with temperature from 5.1×10^5 M^{-1} at 298 K to 4.5×10^5 M^{-1} at 303 K and 3.6×10^5 M^{-1} at 313 K (Table 1), corroborating the static quenching mechanism and indicating high binding strength between the nanoprobe and analyte. Thermodynamic parameters were calculated to elucidate the driving forces and nature of the N,P-CQD-clemastine interaction. The van't Hoff equation, $\ln K_a = -\Delta H^\circ/RT + \Delta S^\circ/R$, was applied by constructing a plot of $\ln K_a$ *versus* $1/T$ (Fig. 2D). Linear regression analysis yielded an enthalpy change (ΔH°) of −9.9 kJ mol^{-1} and entropy change (ΔS°) of 74.6 J mol^{-1} K^{-1}. The negative ΔH° value confirmed that the binding process is exothermic, releasing heat upon complex formation and explaining the decreased stability at elevated temperatures. The positive ΔS° indicated an entropy increase during the interaction, suggesting structural rearrangement and possible release of ordered solvent molecules from the binding interface. Gibbs free energy changes calculated using $\Delta G^\circ = \Delta H^\circ - T\Delta S^\circ$ yielded negative values at all temperatures (−32.2, −32.5, and −33.3 kJ mol^{-1} at 298, 303, and 313 K, respectively; Table 1), demonstrating that the complex formation is thermodynamically spontaneous.

The observed quenching behavior can be rationalized through a detailed examination of the structure–property relationships governing the N,P-CQD-clemastine interaction. The surface chemistry of the N,P-CQDs is directly shaped by the co-doping architecture: nitrogen incorporation introduces pyridinic, pyrrolic, and graphitic nitrogen sites that create electron-rich surface states and modify the electronic band structure, while phosphorus doping generates P═O and P–O–C surface functionalities that increase surface electronegativity and introduce additional energy levels within the bandgap. The synergistic co-doping effect, evidenced by the high quantum yield of 47.2% and the defect-rich carbon framework confirmed by the Raman I_D/I_G ratio of 1.01, creates an electronically active surface with abundant negatively charged functional groups, as quantitatively reflected by the zeta potential of −24.76 mV. This electrochemically active surface is particularly complementary to the molecular architecture of clemastine. Examination of the clemastine structure reveals four distinct interaction-relevant features: the *N*-methyl pyrrolidine group, protonated at the working pH of 8.7 ($pK_a \approx 9.2$), provides a positively charged center that engages in strong electrostatic attraction with the deprotonated carboxylate and phosphate groups on the N,P-CQD surface; the ether oxygen serves as a hydrogen bonding

Table 1 Stern–Volmer quenching constants (K_{sv}), association constants (K_a), and thermodynamic parameters for N,P-CQD-clemastine interaction at three temperatures (298, 303, 313 K)

Temperature (K)	K_{sv} (10^5 M^{-1})	K_a (10^5 M^{-1})	ΔG (kJ mol^{-1})	ΔH (kJ mol^{-1})	ΔS (J mol^{-1} K^{-1})
298	4.3	5.1	−32.2	−9.9	74.6
303	4.0	4.5	−32.5		
313	3.6	3.6	−33.3		

Open Access Article. Published on 27 April 2026. Downloaded on 5/26/2026 1:16:41 AM. This article is licensed under a Creative Commons Attribution-NonCommercial 3.0 Unported Licence.

acceptor interacting with surface hydroxyl and amino groups; the phenyl ring participates in π–π stacking interactions with the graphitic sp^2 carbon domains of the N,P-CQDs; and the electron-withdrawing 4-chlorophenyl substituent further enhances π–π stacking through modification of the aromatic electron density. The negative thermodynamic parameters ($\Delta H^\circ = -9.9$ kJ mol^{-1}, $\Delta G^\circ = -32.2$ to -33.3 kJ mol^{-1}) are fully consistent with this multi-point binding model, where the exothermic character reflects the energetically favorable electrostatic and π-stacking interactions, while the positive entropy change ($\Delta S^\circ = 74.6$ J mol^{-1} K^{-1}) reflects the release of ordered solvent molecules from the binding interface upon complex formation. These structure–property relationships collectively explain both the high binding affinity and the analytical selectivity of the N,P-CQD platform for clemastine determination.

3.3. Optimization of analytical parameters using face-centered central composite design

Face-centered central composite design was employed to systematically optimize the analytical parameters affecting the fluorescence quenching response and to elucidate potential interactions among variables. This response surface methodology enables efficient exploration of the experimental space while minimizing the number of required experiments compared to traditional one-factor-at-a-time approaches. The fluorescence quenching efficiency, expressed as the F_0/F ratio, was selected as the response variable to maximize analytical sensitivity. A second-order polynomial regression model incorporating linear, quadratic, and interaction terms was fitted to the experimental data obtained from the 27-run design matrix (Table S1):

$$Y = \beta_0 + \Sigma\beta_i x_i + \Sigma\beta_{ii} x_i^2 + \Sigma\beta_{ij} x_i x_j + \varepsilon$$

where Y represents the predicted response, β coefficients denote the regression parameters, x_i and x_j are the coded independent variables, and ε is the random error. Statistically insignificant terms ($p > 0.05$) were systematically eliminated through backward elimination to obtain a reduced quadratic model with improved predictive capability.

Analysis of variance confirmed the statistical significance and adequacy of the reduced quadratic model for predicting the fluorescence quenching response (Table 2). The model exhibited a highly significant F-value of 42.89 ($p < 0.0001$), indicating that the observed variation in the response could not be attributed to random noise. Among the individual factors, pH (A), buffer volume (B), and N,P-CQD concentration (C) demonstrated highly significant effects ($p < 0.0001$), while incubation time (D) showed no significant influence and was excluded from the final model. The interaction between pH and buffer volume (AB) and the interaction between pH and N,P-CQD concentration (AC) were both statistically significant ($p = 0.0001$ and $p < 0.0001$, respectively), revealing synergistic effects between these variables. Furthermore, the quadratic terms for pH (A^2) and N,P-CQD concentration (C^2) were significant ($p = 0.0005$), confirming the curvature in the response surface and the existence of optimal values within the experimental range. The lack-of-fit test yielded a non-significant result ($F = 3.20$, $p = 0.2643$), validating that the model adequately described the experimental data without systematic deviation. Model adequacy statistics (Table S2) demonstrated excellent fit quality with a coefficient of determination (R^2) of 0.9405, indicating that 94.05% of the total variation was explained by the model. The adjusted R^2 (0.9186) and predicted R^2 (0.8665) values were in reasonable agreement, with a difference less than 0.2, confirming the model's internal consistency and predictive power. The adequate precision ratio of 21.52, substantially exceeding the minimum threshold of 4, indicated an adequate signal-to-noise ratio for navigating the design space. Diagnostic plots (Fig. S6) further validated model assumptions: the normal probability plot of residuals showed approximate linearity, confirming normal distribution of errors; the predicted *versus* actual plot demonstrated good correlation between experimental and calculated values; the residuals *versus* run number plot revealed random scatter without systematic patterns; and the DFBETAS plot for intercept indicated the absence of influential outliers.

Individual factor effect plots (Fig. 3) revealed distinct response patterns for each variable. The pH exhibited a pronounced quadratic effect with an optimal value near pH 8.7, where the fluorescence quenching efficiency reached

Table 2 Analysis of variance (ANOVA) for the reduced quadratic model obtained from face-centered central composite design optimization

Source	Sum of squares	*df*	Mean square	*F*-value	*p*-value	
Model	57.57	7	8.22	42.89	<0.0001	Significant
A-pH	8.50	1	8.50	44.35	<0.0001	
B-buffer volume	5.98	1	5.98	31.16	<0.0001	
C-N,P CQDs	6.68	1	6.68	34.84	<0.0001	
AB	4.37	1	4.37	22.77	0.0001	
AC	11.75	1	11.75	61.29	<0.0001	
A^2	3.37	1	3.37	17.55	0.0005	
C^2	3.40	1	3.40	17.72	0.0005	
Residual	3.64	19	0.1918			
Lack of fit	3.51	17	0.2067	3.20	0.2643	Not significant
Pure error	0.1292	2	0.0646			
Cor total	61.21	26				

© 2026 The Author(s). Published by the Royal Society of Chemistry

Open Access Article. Published on 27 April 2026. Downloaded on 5/26/2026 1:16:41 AM.
This article is licensed under a Creative Commons Attribution-NonCommercial 3.0 Unported Licence.

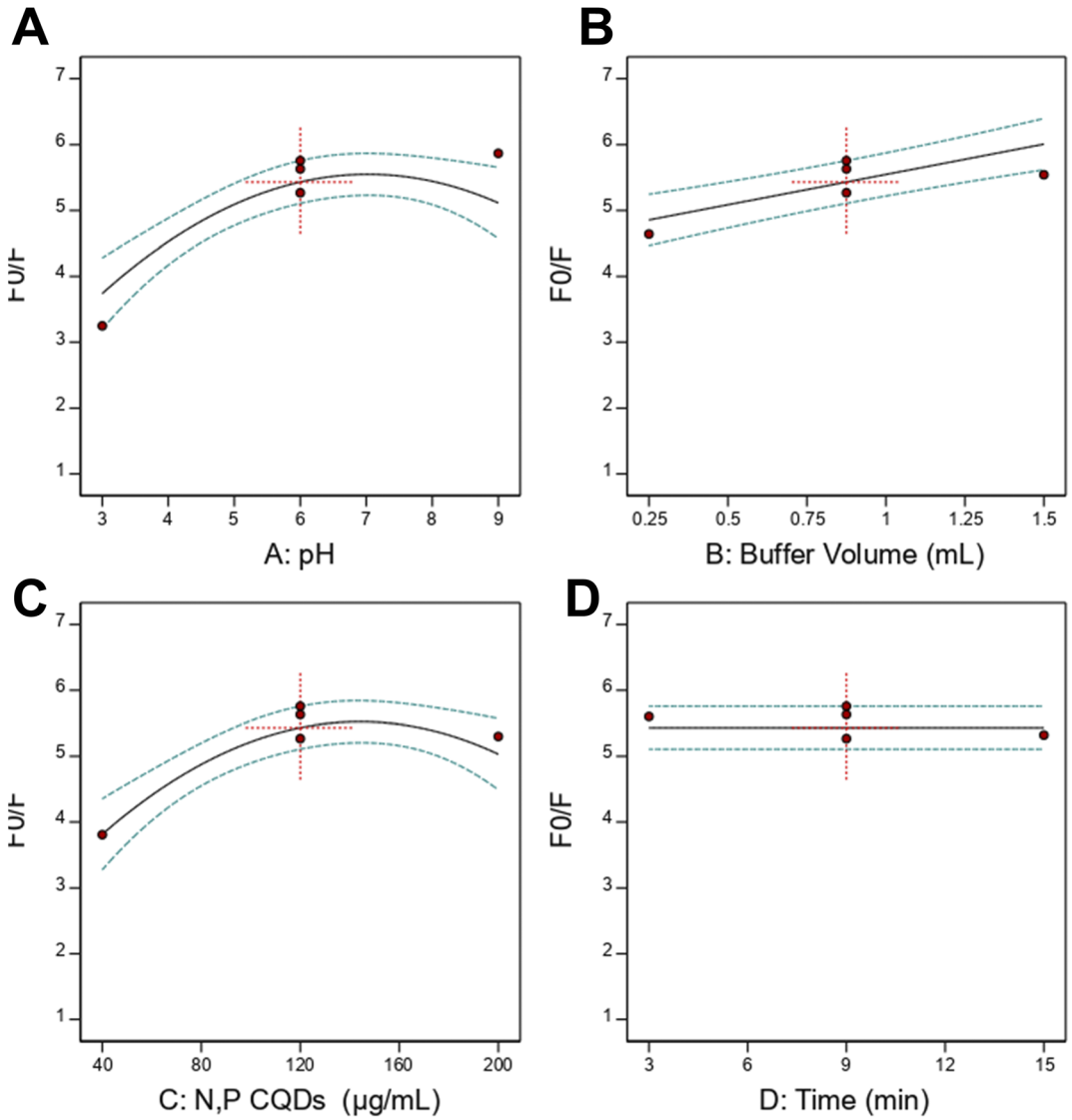

Fig. 3 Individual factor effect plots from face-centered central composite design showing the influence of experimental parameters on fluorescence quenching efficiency. (A) Effect of buffer pH on analytical response. (B) Effect of buffer volume on quenching behavior. (C) Effect of N,P-CQD concentration on fluorescence response. (D) Effect of incubation time on quenching kinetics, demonstrating rapid complex formation consistent with static quenching mechanism.

a maximum. At lower pH values (3–6), the quenching response was substantially diminished due to protonation of carboxyl groups on the N,P-CQD surface, reducing electrostatic attraction with protonated clemastine (Fig. 3A). At highly alkaline pH (>9), the response declined as clemastine deprotonation reduced the positive charge density, weakening ionic interactions. Buffer volume demonstrated a positive linear relationship with the response, achieving maximum quenching efficiency at 1.5 mL (Fig. 3B). This trend reflects the importance of adequate buffering capacity to maintain stable pH during the reaction and ensure reproducible ionization states of both the nanoprobe and analyte. The N,P-CQD concentration displayed a quadratic profile with an optimum around 175 µg mL^{-1}, balancing sufficient fluorophore availability for quenching against potential inner filter effects or aggregation at excessive concentrations (Fig. 3C). Incubation time showed minimal influence on the response within the studied range, suggesting rapid complex formation kinetics, consistent with the static quenching mechanism identified in Section 3.2 (Fig. 3D). Two and three-dimensional response surface plots (Fig. 4) visualized the significant interaction effects. The pH-buffer volume interaction surface (AB interaction) revealed that higher buffer volumes enhanced the quenching response more effectively at intermediate to alkaline pH values, while at acidic pH, buffer volume had negligible impact due to unfavorable ionization conditions. The pH-N,P-CQD concentration interaction surface (AC interaction) demonstrated that optimal nanoprobe concentration shifted depending on pH, with higher concentrations required at suboptimal pH to achieve comparable quenching efficiency. These synergistic interactions underscore

© 2026 The Author(s). Published by the Royal Society of Chemistry

Open Access Article. Published on 27 April 2026. Downloaded on 5/26/2026 1:16:41 AM.
This article is licensed under a Creative Commons Attribution-NonCommercial 3.0 Unported Licence.

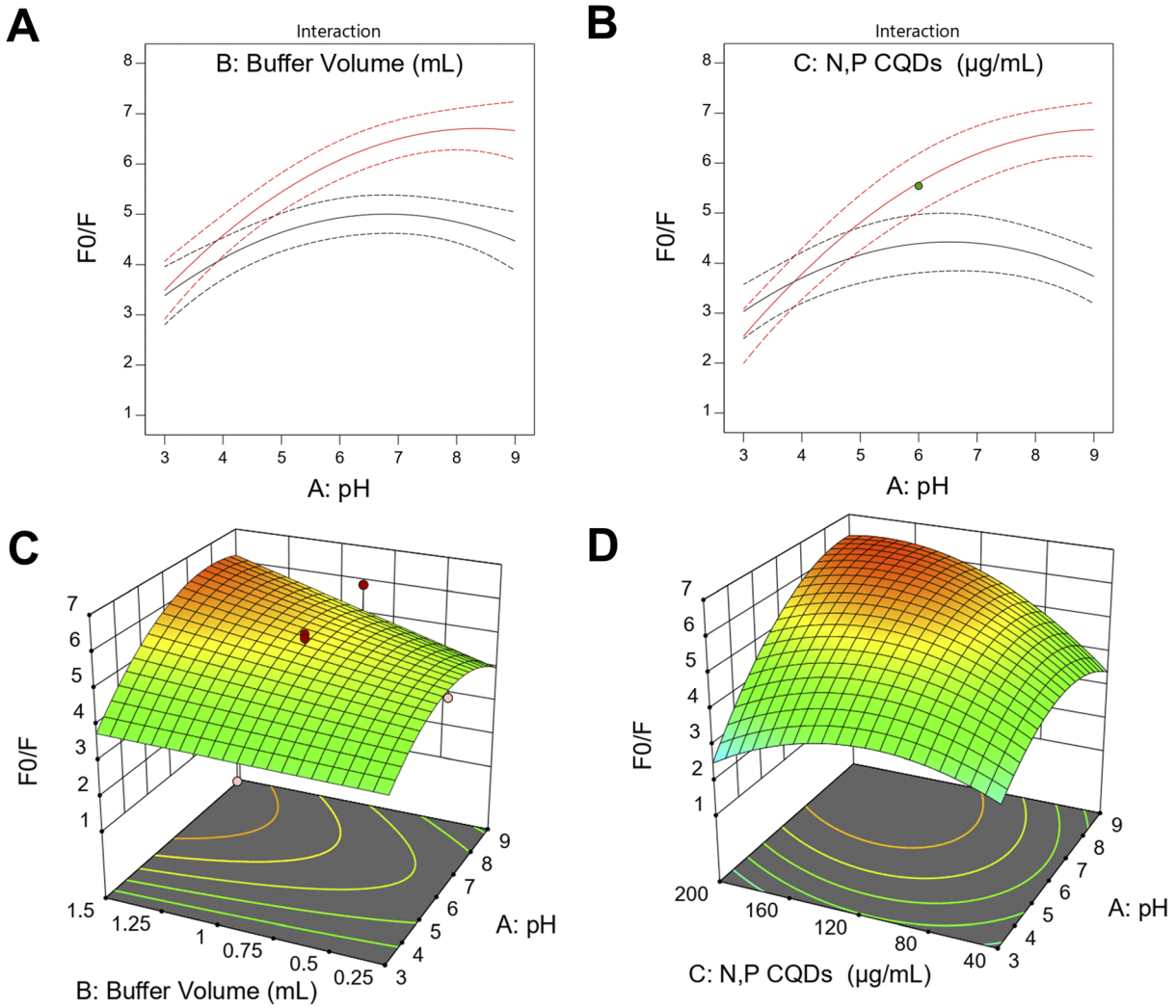

Fig. 4 Two-dimensional interaction plots and three-dimensional response surface visualizations showing significant interaction effects identified by face-centered central composite design. (A) Two-dimensional interaction plot of pH-buffer volume interaction showing interaction curves at different factor levels. (B) Two-dimensional interaction plot of pH-N,P-CQD concentration interaction demonstrating pH-dependent optimal nanoprobe requirements. (C) Three-dimensional response surface of pH-buffer volume interaction providing spatial visualization of synergistic effects on fluorescence quenching efficiency. (D) Three-dimensional response surface of pH-N,P-CQD concentration interaction showing curvature and optimal response region. Color gradients (green to yellow to orange-red) represent fluorescence quenching efficiency (F_0/F ratio values), with warmer colors indicating higher analytical response.

the importance of simultaneous multi-factor optimization rather than sequential univariate approaches.

Numerical optimization was performed using the desirability function approach to identify factor combinations maximizing the fluorescence quenching response while maintaining experimental feasibility. The optimization criteria specified maximizing the F_0/F ratio within the constraints of the experimental ranges. The optimization algorithm converged to the following optimal conditions (Fig. S7): pH 8.67 (rounded to 8.7 for practical application), buffer volume 1.5 mL, N,P-CQD concentration 174.4 µg mL^{-1} (rounded to 175 µg mL^{-1}), and incubation time 3.24 minutes (rounded to 3 minutes). Under these conditions, the model predicted a maximum F_0/F ratio of 6.75. Experimental verification of the optimized conditions yielded an F_0/F value of 6.82 ± 0.15 ($n = 3$), demonstrating excellent agreement with the predicted value and confirming the model's predictive accuracy. Overlay plots (Fig. S8) delineated the design space regions satisfying predetermined criteria for acceptable analytical performance. The yellow-shaded feasible regions in the overlay plots illustrated the operating space where the F_0/F ratio exceeded 6.5, providing guidance for method robustness assessment. The relatively large feasible region indicated that the optimized method exhibits tolerance to minor variations in experimental conditions, contributing to method ruggedness. These optimized parameters were subsequently employed for all validation studies and analytical applications.

3.4. Analytical performance and method validation

The developed spectrofluorimetric method was thoroughly validated according to ICH Q2(R2) guidelines to assess its

© 2026 The Author(s). Published by the Royal Society of Chemistry

Open Access Article. Published on 27 April 2026. Downloaded on 5/26/2026 1:16:41 AM. This article is licensed under a Creative Commons Attribution-NonCommercial 3.0 Unported Licence.

suitability for quantitative determination of clemastine in pharmaceutical formulations and biological matrices. Under optimized conditions, a linear relationship was established between the fluorescence quenching response (F_0/F) and clemastine concentration over the range of 0.1–4.0 μg mL^{-1} (Table 3). Linear regression analysis yielded the equation: F_0/F = 1.4782[Clemastine] + 0.9222, with correlation coefficient (r^2) of 0.9997, demonstrating strong linearity across the working range. The limit of detection (LOD) and limit of quantification (LOQ), calculated as $3.3\sigma/S$ and $10\sigma/S$ respectively (where σ is the standard deviation of the blank response and S is the slope of the calibration curve), were 0.03 and 0.09 μg mL^{-1}, indicating high sensitivity suitable for trace-level analysis. Method accuracy was evaluated by analyzing clemastine standards at three concentration levels (1.0, 2.0, and 3.0 μg mL^{-1}) in triplicate, yielding mean recovery of 100.41 ± 1.12%, confirming the absence of systematic bias (Table 3). Precision studies demonstrated excellent reproducibility, with repeatability precision (intra-day, $n = 9$) showing a relative standard deviation (RSD) of 1.11% and intermediate precision (inter-day over three consecutive days, $n = 9$) exhibiting an RSD of 1.62% (Table 3). Both precision values were well below the 2% acceptance threshold, indicating consistent analytical performance.

Method robustness was assessed by introducing small deliberate variations in critical parameters while maintaining other factors constant (Table 3). Minor changes in buffer pH (8.5, 8.7, 8.9), N,P-CQD concentration (170, 175, 180 μg mL^{-1}), and reaction time (2.5, 3.0, 3.5 min) resulted in recovery values of 98.14 ± 1.27%, 99.78 ± 1.70%, and 101.88 ± 1.57%, respectively, demonstrating that the method remained reliable despite minor operational variations. Selectivity was rigorously evaluated by examining potential interference from common pharmaceutical excipients and endogenous biological components (Table S3). Seven pharmaceutical excipients typically present in tablet formulations (microcrystalline cellulose, lactose monohydrate, magnesium stearate, polyethylene glycol, hypromellose, croscarmellose sodium, and colloidal silicon dioxide) at concentrations equivalent to 100 μg mL^{-1} showed no significant interference, with quenching efficiency values (QE%) ranging from 80.14% to 82.98% remaining comparable to clemastine alone (81.32%), and RSD values below 2.1%. Similarly, seven endogenous biological substances (glucose, urea, uric acid, creatinine, albumin, ascorbic acid, and cholesterol) at concentrations 10-fold higher than physiological levels exhibited no interference, with QE% values between 80.04% and 83.90% closely matching the response of clemastine alone, and RSD values below 2.2%. Besides, the selectivity of the method was further validated against structurally related H1-antihistamines, diphenhydramine hydrochloride and chlorpheniramine maleate, at 10-fold excess concentration (10 μg mL^{-1}). Both compounds exhibited no significant interference, with QE% values of 82.34% and 81.89% remaining comparable to clemastine alone (81.32%), and RSD values below 2.2% (Table S3), confirming the high selectivity of the method for clemastine determination in the presence of structurally related compounds. These findings confirmed the method's high selectivity and freedom from matrix effects, ensuring accurate quantification of clemastine in complex pharmaceutical and biological matrices.

Table 3 Analytical performance parameters and method validation results for clemastine determination according to ICH Q2(R2) guidelines

Parameters		Clemastine
Excitation wavelength (nm)		345
Emission wavelength (nm)		445
Linearity range (μg mL^{-1})		0.1–4.0
Slope		1.4782
Intercept		0.9222
Correlation coefficient (r^2)		0.9997
LOD (μg mL^{-1})		0.03
LOQ (μg mL^{-1})		0.09
Accuracy (% R)[a]		100.41 ± 1.116
Repeatability precision (% RSD)[b]		1.111
Intermediate precision (% RSD)[c]		1.618
Robustness (% R)	Buffer (pH)	98.14 ± 1.266
	N,P CQDs conc. (μg mL^{-1})	99.78 ± 1.695
	Reaction time (min)	101.88 ± 1.565

[a] Average of 9 determinations (3 concentrations repeated 3 times). [b] % RSD of 9 determinations (3 concentrations repeated 3 times) measured on the same day. [c] % RSD of 9 determinations (3 concentrations repeated 3 times) measured in the three consecutive days.

3.5. Application to real sample analysis

The validated method was successfully applied to the determination of clemastine in synthetic pharmaceutical tablet formulations prepared with representative excipient compositions. To assess the reliability and performance of the developed spectrofluorimetric method relative to established analytical procedures, a statistical comparison was conducted against a reported HPLC method by analyzing the same pharmaceutical samples (Table 4). Five replicate determinations of clemastine in the synthetic tablets yielded a mean recovery of 99.80 ± 1.37% using the developed method, while the reported HPLC method gave 100.08 ± 0.76% (Table 4). Student's t-test was applied to evaluate whether the two methods produced significantly different mean values. The calculated t-value of 0.411 was substantially lower than the critical tabulated value of 2.306 at the 95% confidence level ($p = 0.695$), indicating no significant difference between the methods in terms of accuracy (Table 4). The F-test was employed to compare the precision of both methods by examining the variance ratio. The calculated F-value of 3.242 did not exceed the critical tabulated value of 6.338 ($p = 0.281$), demonstrating comparable precision between the two analytical approaches (Table 4). Furthermore, equivalence testing was performed to assess whether the methods were not only statistically similar but also practically equivalent within predefined acceptance limits of ±2% bias. The calculated equivalence interval ($\theta_L = -1.906$, $\theta_U = 1.329$) fell entirely within the acceptable range of ±2%, confirming practical equivalence between the developed and reported methods (Table 4). These comprehensive statistical evaluations validated that the proposed spectrofluorimetric method provides

Open Access Article. Published on 27 April 2026. Downloaded on 5/26/2026 1:16:41 AM.
This article is licensed under a Creative Commons Attribution-NonCommercial 3.0 Unported Licence.

Table 4 Statistical comparison between the developed spectrofluorimetric method and reported HPLC method for clemastine fumarate determination in synthetic pharmaceutical tablets

Method	Mean[a]	SD	t-test (2.306)[b]	P value	F-value (6.338)[b]	P value	θ_L[c]	θ_U[c]
Developed method	99.80	1.371	0.411	0.695	3.242	0.281	−1.906	1.329
Reported method	100.08	0.762						

[a] Average of five determinations. [b] The values in parenthesis are tabulated values of "t"and "F" at ($P = 0.05$). [c] Bias of ± 2% is acceptable.

accuracy and precision equivalent to the established chromatographic approach while offering advantages of simplicity, rapidity, and lower operational costs for quality control analysis of clemastine-containing formulations.

The method's applicability to biological matrices was evaluated through recovery studies in spiked human plasma samples at four concentration levels (Table 5). Clemastine was spiked into blank plasma at concentrations of 0.2, 0.5, 1.0, and 2.0 μg mL^{-1}, and analyzed following protein precipitation and sample preparation procedures. Recovery values ranged from 96.81% to 104.52% across all concentration levels, with RSD values between 2.33% and 3.32% ($n = 3$). The recoveries at lower concentrations (0.2 and 0.5 μg mL^{-1}) were 104.52% and 102.25%, respectively, while those at higher concentrations (1.0 and 2.0 μg mL^{-1}) were 96.81% and 98.50%, demonstrating acceptable accuracy throughout the tested range. The slightly higher RSD values in plasma compared to standard solutions reflect the increased complexity of the biological matrix, yet all values remained below 4%, confirming satisfactory precision for bioanalytical applications. These results established the method's suitability for pharmacokinetic studies and therapeutic drug monitoring of clemastine in human plasma.

3.6. Green analytical chemistry assessment

The environmental sustainability and practical applicability of the developed spectrofluorimetric method were comprehensively evaluated using multiple complementary greenness assessment tools, including the Modified Green Analytical Procedure Index (MOGAPI), Carbon Footprint Reduction Index (CaFRI), Blue Applicability Grade Index (BAGI), and White Analytical Chemistry (WAC) RGB12 model (Fig. 5). These metrics provide holistic evaluation across environmental impact, analytical performance, and practical feasibility dimensions, enabling objective assessment of the method's sustainability profile.

The MOGAPI evaluation yielded a total score of 76 (Fig. 5A), classifying the method as "excellent green" according to the established threshold of ≥75. The pentagram pictogram revealed several environmentally favorable aspects, indicated by green-colored subsections, particularly in energy consumption, occupational safety, and waste management categories. The method consumed minimal energy (≤0.1 kWh per sample) due to the use of low-power spectrofluorometric instrumentation and short analysis time. Hermetic sealing of the analytical process eliminated direct operator exposure to reagents, enhancing laboratory safety. Waste generation remained below 10 mL per sample, with appropriate waste treatment protocols implemented. However, moderate performance was observed in certain aspects, as indicated by yellow subsections, including the use of non-green organic solvents during sample extraction and the requirement for off-line sample collection and transport. Red subsections highlighted areas requiring improvement, notably the macro-extraction scale and the necessity of chemical preservation. Despite these limitations, the overall excellent score confirmed the method's strong environmental credentials and alignment with green analytical chemistry principles.

Carbon footprint assessment *via* the CaFRI metric produced a score of 78 (Fig. 5B), demonstrating favorable sustainability from a climate impact perspective. The foot-shaped pictogram exhibited predominantly green sections, particularly in energy-related criteria, CO_2 emissions, sample storage, waste generation, and reagent consumption. The method's low electrical power requirement (<0.1 kW) and favorable emission factor (<0.1 kg CO_2 per kWh) contributed significantly to reduced carbon footprint. Minimal waste generation (<10 mL per sample), limited hazard pictograms (≤3), and small organic solvent volumes (<5 mL per sample) further enhanced the environmental profile. Yellow sections indicated moderate performance in transportation distance (1–10 miles between field and laboratory) and the necessity of energy-intensive non-analytical equipment for sample preparation. Red sections identified opportunities for improvement, specifically the absence of solvent recycling protocols, reliance on manual operation rather than automation, and lack of eco-friendly transportation vehicles. Nevertheless, the high overall score confirmed that the method maintains a relatively low carbon footprint compared to conventional analytical approaches.

The BAGI assessment yielded a score of 72.5 (Fig. 5C), exceeding the recommended threshold of 60 and confirming the method's practical applicability for routine analytical applications. The star-shaped pictogram displayed predominantly dark blue sections, indicating high compliance in multiple attributes including analysis type (quantitative), sample throughput (>10 samples per hour), simultaneous

Table 5 Recovery studies of clemastine in spiked human plasma samples at four concentration levels ($n = 3$)

Spiked (μg mL^{-1})	Found (μg mL^{-1})	Recovery (%)	RSD ($n = 3$, %)
0.2	0.209	104.52	2.776
0.5	0.511	102.25	3.323
1.0	0.968	96.81	2.335
2.0	1.970	98.50	2.33

© 2026 The Author(s). Published by the Royal Society of Chemistry

Open Access Article. Published on 27 April 2026. Downloaded on 5/26/2026 1:16:41 AM.
This article is licensed under a Creative Commons Attribution-NonCommercial 3.0 Unported Licence.

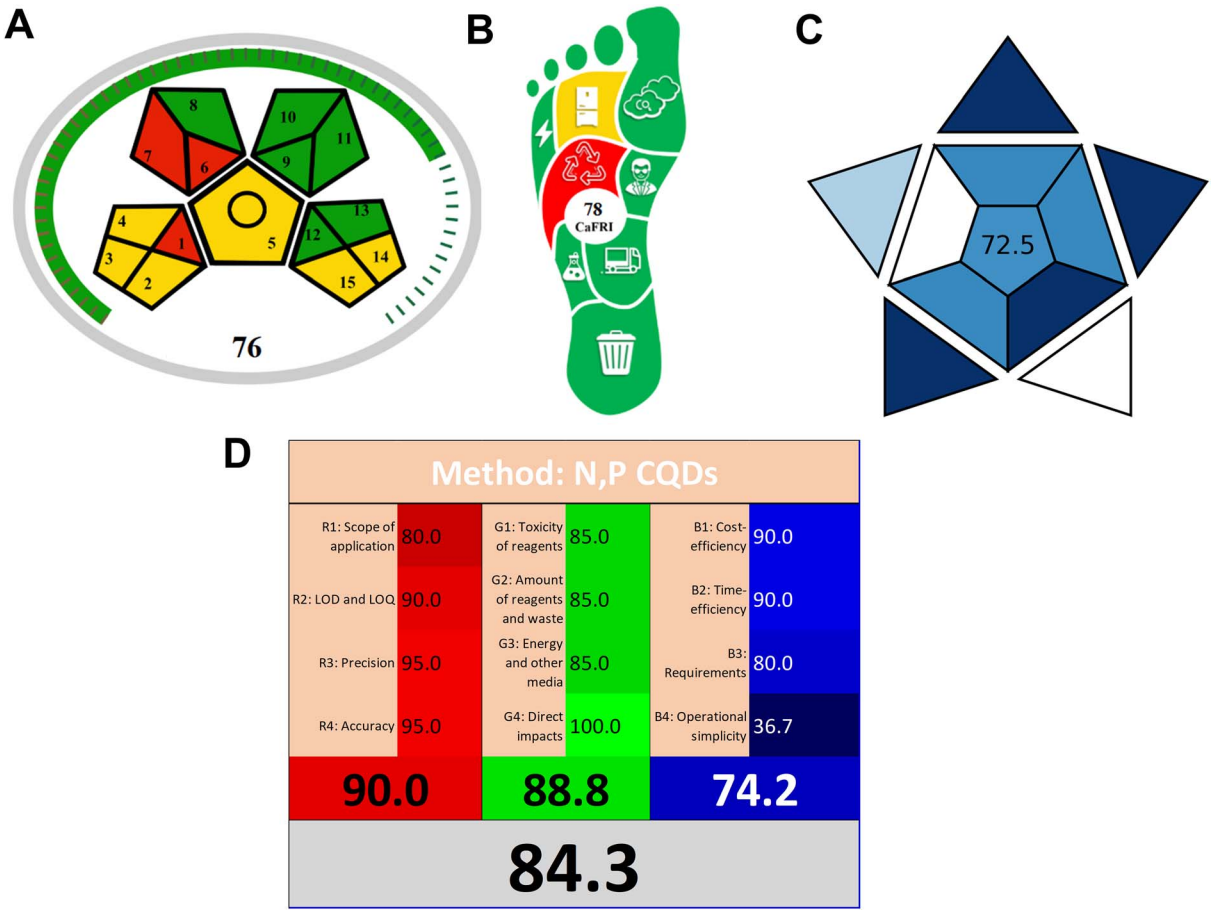

Fig. 5 Comprehensive green analytical chemistry assessment of the developed spectrofluorimetric method for clemastine fumarate determination using multiple sustainability metrics. (A) MOGAPI pictogram with subsections color-coded as green (satisfactory), yellow (moderate), and red (requires improvement). (B) CaFRI foot-shaped pictogram displaying environmental performance across eight criteria categories. (C) BAGI star-shaped pictogram demonstrating practical applicability across ten attributes with varying compliance levels. (D) RGB12 White Analytical Chemistry model showing red (analytical efficiency), green (environmental friendliness), blue (practical efficiency), and overall whiteness score for balanced sustainability assessment.

sample preparation capacity (>95), sample preparation simplicity, and minimal sample volume requirements. The absence of preconcentration requirements and availability of simple spectrofluorometric instrumentation contributed to high practicality scores. Light blue sections indicated moderate performance in reagent availability, as the N,P-CQD nanoprobes require in-laboratory synthesis rather than commercial procurement. The manual nature of the analysis also limited the automation attribute score. Despite these constraints, the overall score confirmed that the method offers substantial practical advantages for implementation in analytical laboratories.

The comprehensive RGB12 model provided balanced evaluation across analytical (red), environmental (green), and practical (blue) dimensions (Fig. 5D). The analytical efficiency component achieved an excellent score of 90.0, reflecting the method's broad scope of application, low detection and quantification limits, high precision, and accurate quantification. The environmental friendliness component scored 88.8, indicating strong performance in minimizing reagent toxicity, waste generation, and energy consumption, with perfect scores achieved for direct environmental impacts such as the absence of animal testing. The practical efficiency component scored 74.2, demonstrating good cost-effectiveness and time-efficiency, though somewhat limited by operational simplicity considerations related to manual analysis and nanoprobe synthesis requirements. The overall whiteness score of 84.3 confirmed that the method achieves excellent synergy across all three fundamental dimensions of analytical method quality.

A critical comparison of the environmental sustainability profile of the developed method with existing analytical approaches for clemastine determination reveals several distinct advantages. The reported HPLC method by Ingole *et al.* employs a mobile phase comprising 90% methanol, generating substantial volumes of organic solvent waste per analysis and requiring energy-intensive pumping systems and column conditioning procedures. Similarly, the LC-MS/MS method, while highly sensitive, demands extensive organic solvent consumption during both mobile phase preparation and liquid–liquid extraction, in addition to the significant energy

Open Access Article. Published on 27 April 2026. Downloaded on 5/26/2026 1:16:41 AM. This article is licensed under a Creative Commons Attribution-NonCommercial 3.0 Unported Licence.

requirements of mass spectrometric instrumentation. Among the fluorimetric approaches, the NBD-Cl derivatization method requires toxic chlorinated reagents and multi-step derivatization procedures generating hazardous waste, while the eosin Y fluorescence quenching method involves organic dye reagents with associated disposal concerns. In contrast, the developed N,P-CQD-based method employs water as the primary solvent for the analytical determination step, eliminates chemical derivatization entirely, and utilizes energy-efficient spectrofluorometric instrumentation with minimal waste generation per sample. Nevertheless, certain trade-offs warrant acknowledgment for a balanced assessment. The requirement for in-laboratory synthesis of N,P-CQDs adds a preparatory step not present in methods utilizing commercially available reagents. The use of organic solvents during sample extraction and protein precipitation for plasma analysis partially offsets the environmental advantages at the sample preparation stage. Furthermore, the manual nature of the analytical procedure limits throughput compared to automated chromatographic systems. Despite these limitations, the comprehensive green chemistry assessment using MOGAPI, CaFRI, BAGI, and RGB12 metrics confirms that the overall environmental burden of the developed method remains substantially lower than conventional chromatographic approaches, representing a meaningful advancement toward sustainable pharmaceutical analysis.

4. Conclusion

This study successfully developed and validated a novel spectrofluorimetric method utilizing microwave-assisted nitrogen and phosphorus co-doped carbon quantum dots as fluorescent nanoprobes for the sensitive and selective determination of clemastine in pharmaceutical formulations and biological matrices. The N,P-CQDs were synthesized *via* a rapid, energy-efficient microwave approach, yielding nanoprobes with excellent quantum yield (47.2 ± 2.3%), uniform size distribution (3.2 ± 0.9 nm), and strong blue fluorescence emission. Face-centered central composite design enabled systematic optimization of analytical parameters, while mechanistic investigations confirmed static quenching through ground–state complex formation driven by electrostatic interactions and hydrogen bonding. The validated method demonstrated excellent analytical performance including wide linearity (0.1–4.0 μg mL^{-1}, r^2 = 0.9997), high sensitivity (LOD = 0.03 μg mL^{-1}), satisfactory accuracy (100.41 ± 1.12%), and robust precision (RSD < 2%). Successful application to synthetic pharmaceutical tablets and spiked human plasma samples, combined with statistical equivalence to established HPLC methods, confirmed the method's reliability. Comprehensive green chemistry assessment using MOGAPI (76), CaFRI (78), BAGI (72.5), and RGB12 (whiteness = 84.3) demonstrated outstanding environmental sustainability and balanced performance.

Despite these achievements, certain limitations warrant acknowledgment. The method employs off-line sample collection and macro-scale extraction procedures, presenting opportunities for miniaturization and automation. The use of non-green organic solvents during sample preparation and the absence of solvent recycling protocols represent areas requiring further optimization to enhance environmental performance. The manual nature of the analytical procedure limits throughput compared to fully automated systems. Additionally, the fluorescence quenching mechanism based on non-specific electrostatic and hydrogen bonding interactions may limit selectivity when analyzing complex matrices containing structurally similar compounds or multiple cationic species, potentially requiring chromatographic separation prior to detection in highly complex samples. Furthermore, the bioanalytical validation was demonstrated using spiked human plasma samples rather than authentic patient samples, and direct comparison with LC-MS/MS methodology in real biological matrices was not performed due to instrumentation constraints. Future research should focus on developing scaled-up synthesis protocols for commercial N,P-CQD production, integrating miniaturized sample preparation techniques to reduce solvent consumption, implementing flow injection or microfluidic platforms for automation, exploring green solvent alternatives, extending the method to simultaneous multi-analyte determination of related antihistamines, and clinical validation using patient-derived samples and cross-validation against LC-MS/MS to further establish the method's bioanalytical reliability for therapeutic drug monitoring applications. Incorporation of molecular imprinting techniques or surface functionalization strategies could enhance selectivity for clemastine recognition. Overall, the proposed method provides a practical, cost-effective, and green alternative to conventional chromatographic techniques, contributing to the ongoing evolution toward sustainable pharmaceutical analysis and supporting the global transition to greener analytical practices in quality control and clinical laboratories.

Conflicts of interest

There are no conflicts to declare.

Data availability

The authors confirm that the data supporting the findings of this study are available within the article and its supplementary information (SI). Any additional data are available from the corresponding author upon reasonable request. Supplementary information is available. See DOI: https://doi.org/10.1039/d6ra01896c.

Acknowledgements

The authors extend their appreciation for Princess Nourah bint Abdulrahman University Researchers Supporting Project number (PNURSP2026R917), Princess Nourah bint Abdulrahman University, Riyadh, Saudi Arabia.

© 2026 The Author(s). Published by the Royal Society of Chemistry

Open Access Article. Published on 27 April 2026. Downloaded on 5/26/2026 1:16:41 AM. This article is licensed under a Creative Commons Attribution-NonCommercial 3.0 Unported Licence.

References

1 X. Xu, R. Ray, Y. Gu, H. J. Ploehn, L. Gearheart, K. Raker and W. A. Scrivens, *J. Am. Chem. Soc.*, 2004, **126**, 12736–12737.
2 N. Azam, M. Najabat Ali and T. Javaid Khan, *Front. Mater.*, 2021, **8**, 700403.
3 N. A. Pechnikova, K. Domvri, K. Porpodis, M. S. Istomina, A. V. Iaremenko and A. V. Yaremenko, *Aggregate*, 2025, **6**, e707.
4 A. Salvi, S. Kharbanda, P. Thakur, M. Shandilya and A. Thakur, *Carbon Trends*, 2024, **17**, 100407.
5 F. Belal, M. Mabrouk, S. Hammad, H. Ahmed and A. Barseem, *J. Fluoresc.*, 2024, **34**, 119–138.
6 Y. Gao, J. Wang, X. Mu, B. Liu, M. Xia, F. Wang and Z. Tong, *Talanta*, 2025, 128066.
7 H. Kaurav, D. Verma, A. Bansal, D. N. Kapoor and S. Sheth, *Front. Chem.*, 2023, **11**, 1227843.
8 S. R. Lodha, J. G. Merchant, A. J. Pillai, A. H. Gore, P. O. Patil, S. N. Nangare, G. G. Kalyankar, S. A. Shah, D. R. Shah and S. P. Patole, *Heliyon*, 2024, 10.
9 E. W. Idan, B. Qasim and J. N. Jeber, *J. Fluoresc.*, 2025, 1–19.
10 P. Zuo, Z. Chen, F. Yu, J. Zhang, W. Zuo, Y. Gao and Q. Liu, *RSC Adv.*, 2020, **10**, 32919–32926.
11 H. Li, X. He, Y. Liu, H. Yu, Z. Kang and S.-T. Lee, *Mater. Res. Bull.*, 2011, **46**, 147–151.
12 A. Sethulekshmi, A. Aparna, P. Parvathi, R. Pathak, V. D. Punetha, M. Selvaraj and S. Appukuttan, *Chem. Eng. J.*, 2025, 163262.
13 Q. Xu, B. Li, Y. Ye, W. Cai, W. Li, C. Yang, Y. Chen, M. Xu, N. Li and X. Zheng, *Nano Res.*, 2018, **11**, 3691–3701.
14 F.-J. Cao, X. Hou, K.-F. Wang, T.-Z. Jin and H. Feng, *RSC Adv.*, 2023, **13**, 21088–21095.
15 R. Bao, Z. Chen, Z. Zhao, X. Sun, J. Zhang, L. Hou and C. Yuan, *Nanomaterials*, 2018, **8**, 386.
16 V. Magesh, A. K. Sundramoorthy and D. Ganapathy, *Front. Mater.*, 2022, **9**, 906838.
17 B. I. Salman, A. I. Hassan, Y. F. Hassan, R. E. Saraya and H. A. Batakoushy, *J. Fluoresc.*, 2023, **33**, 1101–1110.
18 N. A. Qandeel, A. A. El-Masry, M. Eid, M. A. Moustafa and R. El-Shaheny, *Anal. Chim. Acta*, 2023, **1237**, 340592.
19 S. Soni and G. Kaur, *Naunyn-Schmiedeberg's Arch. Pharmacol.*, 2025, 1–14.
20 H. F. Schran, L. Petryk, C. T. Chang, R. O'Connor and M. B. Gelbert, *J. Clin. Pharmacol.*, 1996, **36**, 911–922.
21 A. J. Green, J. M. Gelfand, B. A. Cree, C. Bevan, W. J. Boscardin, F. Mei, J. Inman, S. Arnow, M. Devereux and A. Abounasr, *The Lancet*, 2017, **390**, 2481–2489.
22 L. Ingole, *Res. J. Pharm. Dosage Forms Technol.*, 2019, **11**, 87–94.
23 J. E. Conte, G. Wang, E. T. Lin and E. Zurlinden, *J. Chromatogr. B Biomed. Sci. Appl.*, 2001, **753**, 343–353.
24 M. M. Bedair, M. A. Korany and A. S. Issa, *Analyst*, 1988, **113**, 1137–1138.
25 S. S. Abd El-Hay, M. Y. El-Mammli and A. A. Shalaby, *Arab. J. Chem.*, 2016, **9**, S541–S547.
26 S. S. Abd El-Hay, C. L. Colyer, W. S. Hassan and A. Shalaby, *J. AOAC Int.*, 2013, **96**, 968–975.
27 M. A. Abdel-Lateef, I. A. Darwish, H. Gomaa and N. S. Katamesh, *J. Fluoresc.*, 2025, **35**, 2773–2784.
28 F. R. Mansour, J. Płotka-Wasylka and M. Locatelli, *Analytica*, 2024, **5**, 451–457.
29 F. R. Mansour and P. M. Nowak, *BMC Chem.*, 2025, **19**, 121.
30 N. Manousi, W. Wojnowski, J. Płotka-Wasylka and V. Samanidou, *Green Chem.*, 2023, **25**, 7598–7604.
31 P. M. Nowak, R. Wietecha-Posłuszny and J. Pawliszyn, *TrAC, Trends Anal. Chem.*, 2021, **138**, 116223.
32 K. M. Omer, D. I. Tofiq and A. Q. Hassan, *Microchim. Acta*, 2018, **185**, 466.
33 A. H. Kamal, R. E. Kannouma, M. A. Hammad and F. R. Mansour, *Microchem. J.*, 2024, **206**, 111488.

© 2026 The Author(s). Published by the Royal Society of Chemistry